

---

---

# Multifunctional Imaging Signature for V-KI-RAS2 Kirsten Rat Sarcoma Viral Oncogene Homolog (KRAS) Mutations in Colorectal Cancer

Kenneth A. Miles<sup>1</sup>, Balaji Ganeshan<sup>1</sup>, Manuel Rodriguez-Justo<sup>1</sup>, Vicky J. Goh<sup>2</sup>, Zia Ziauddin<sup>1</sup>, Alec Engledow<sup>1</sup>, Marie Meagher<sup>1</sup>, Raymondo Endozo<sup>1</sup>, Stuart A. Taylor<sup>1</sup>, Stephen Halligan<sup>1</sup>, Peter J. Ell<sup>1</sup>, and Ashley M. Groves<sup>1</sup>

<sup>1</sup>University College London/UCLH, London, United Kingdom; and <sup>2</sup>Imaging Sciences, KCL, Lambeth Wing, St Thomas's Hospital, London United Kingdom

---

This study explores the potential for multifunctional imaging to provide a signature for V-KI-RAS2 Kirsten rat sarcoma viral oncogene homolog (KRAS) gene mutations in colorectal cancer. **Methods:** This prospective study approved by the institutional review board comprised 33 patients undergoing PET/CT before surgery for proven primary colorectal cancer. Tumor tissue was examined histologically for presence of the KRAS mutations and for expression of hypoxia-inducible factor-1 (HIF-1) and minichromosome maintenance protein 2 (mcm2). The following imaging parameters were derived for each tumor: <sup>18</sup>F-FDG uptake (<sup>18</sup>F-FDG maximum standardized uptake value [SUV<sub>max</sub>]), CT texture (expressed as mean of positive pixels [MPP]), and blood flow measured by dynamic contrast-enhanced CT. A recursive decision tree was developed in which the imaging investigations were applied sequentially to identify tumors with KRAS mutations. Monte Carlo analysis provided mean values and 95% confidence intervals for sensitivity, specificity, and accuracy. **Results:** The final decision tree comprised 4 decision nodes and 5 terminal nodes, 2 of which identified KRAS mutants. The true-positive rate, false-positive rate, and accuracy (95% confidence intervals) of the decision tree were 82.4% (63.9%–93.9%), 0% (0%–10.4%), and 90.1% (79.2%–96.0%), respectively. KRAS mutants with high <sup>18</sup>F-FDG SUV<sub>max</sub> and low MPP showed greater frequency of HIF-1 expression ( $P = 0.032$ ). KRAS mutants with low <sup>18</sup>F-FDG SUV<sub>max</sub>, high MPP, and high blood flow expressed mcm2 ( $P = 0.036$ ). **Conclusion:** Multifunctional imaging with PET/CT and recursive decision-tree analysis to combine measurements of tumor <sup>18</sup>F-FDG uptake, CT texture, and perfusion has the potential to identify imaging signatures for colorectal cancers with KRAS mutations exhibiting hypoxic or proliferative phenotypes.

**Key Words:** KRAS protein; human; diagnostic imaging; colonic neoplasms; comparative study

**J Nucl Med 2014; 55:386–391**

DOI: 10.2967/jnumed.113.120485

---

**A**pproximately 30%–40% of colorectal cancers (CRCs) exhibit a mutation in the V-KI-RAS2 Kirsten rat sarcoma viral oncogene

homolog (KRAS) (1). The presence of a KRAS mutation has clinical significance because of an association with resistance to drugs that target the epidermal growth factor receptor (EGFR) (2). Determination of KRAS mutational status is usually via histologic examination of tumor tissue. However, histologic approaches have limitations that generate a need for more comprehensive approaches including correlative imaging techniques. One limitation of histologic evaluations is heterogeneity of KRAS mutational status, which can be either intratumoral or between tumor sites and occurs in approximately 10% of cases (3–5). Heterogeneity can be problematic for neoadjuvant treatment, where the KRAS mutational status is determined from biopsy material rather than the whole resected specimen. As a result, discordant rates of up to 12.5% between biopsy and resected tumor assessments have been reported, approximating the incidence of KRAS mutational heterogeneity (6–8), although discordant rates may be lower with more recent analysis methods (9). Failure to determine KRAS mutational status due to poor DNA quality in the tissue sample represents a further limitation of histologic analysis that can occur in 6% and 9% of cases (10). Identification of an imaging signature for the KRAS mutation would potentially allow imaging to provide an adjunct to histologic assessment by enabling simultaneous evaluation of the whole tumor and multiple tumor sites and by providing an indication of KRAS mutation status when tissue sampling has failed. Furthermore, by identifying tumor phenotype (which determines tumor behavior), imaging evaluations of KRAS mutational status could potentially predict resistance to EGFR targeting agents more accurately than genetic analysis.

Imaging identification of KRAS mutations in CRC has received little attention to date. The use of <sup>68</sup>Ga-labeled oligonucleotides for PET has been proposed but has not been reported in humans (11). A single human PET study with 51 cases has shown increased accumulation of <sup>18</sup>F-FDG in CRCs exhibiting the KRAS mutation, but the reported accuracy was insufficient for reliable clinical assessment of mutational status (12). Laboratory investigations have suggested a synergistic interaction between KRAS activity, tumor hypoxia, and angiogenesis (13–15). Combined PET imaging of CRC tumor metabolism and imaging of perfusion with CT has recently been shown to reflect the expression of hypoxia inducible factor-1 (HIF-1) and vascular endothelial growth factor, biomolecules that modulate tumor responses to hypoxia and promotion of angiogenesis, respectively (16). There is also emerging evidence that CT assessments of tumor texture may reflect angiogenesis and hypoxia in CRC and non-small cell lung cancer (17,18). Hence a combination of these imaging biomarkers could potentially provide an

Received Jan. 23, 2013; revision accepted Sep. 12, 2013.

For correspondence or reprints contact: Ashley M. Groves, Institute of Nuclear Medicine University College London, UCH 235, Euston Rd., 5th Fl., London, United Kingdom NW1 2BU.

E-mail: ashleygroves@nhs.net

Published online Feb. 10, 2014.

COPYRIGHT © 2014 by the Society of Nuclear Medicine and Molecular Imaging, Inc.

imaging signature for the KRAS mutation. The feasibility of acquiring this combination of imaging parameters has been confirmed (17–20), but methods for determining the optimal way of combining multiple imaging biomarkers are underdeveloped. One approach increasingly used in genetic research entails recursive decision-tree analysis, which can model the sequential application of predictive biomarkers and evaluate overall performance (21). This initial exploratory study therefore uses decision-tree analysis to determine the potential for multiparametric PET/CT to identify KRAS mutations in CRC.

## MATERIALS AND METHODS

### Patients

Approval from the institutional review board and informed consent were obtained for this prospective study. Recruits comprised all patients for whom histologic data demonstrating KRAS mutation status were available from a larger study of 60 patients sequentially undergoing combined <sup>18</sup>F-FDG PET/dynamic contrast-enhanced (DCE) CT before surgery for proven primary CRC for whom no contraindications to <sup>18</sup>F-FDG PET (uncontrolled diabetes) or administration of contrast material were present (renal impairment, previous allergy). Thirty-three patients were included, of whom 20 patients were men and 13 women (mean age ± SD, 64.4 ± 10.5 y). Of the 27 patients excluded, 22 had undergone chemoradiotherapy before surgery, making determination of KRAS status unreliable. In the remaining 5 excluded patients, histologic determination of KRAS status failed. Different subsets of the same larger cohort had formed the basis of 3 previous published studies that did not entail analysis of KRAS mutational status (16,22,23).

### Histopathologic Analysis

After surgical resection, specimens were fixed in 10% neutral-buffered formalin solution. The tumor blocks were processed in a conventional manner and embedded into paraffin wax. Sections 4-μm thick were obtained from each tissue block and routinely stained with hematoxylin and eosin. The KRAS status was analyzed either by pyrosequencing analysis (in-house design) of tumor tissue for codons 12, 13, and 61 of KRAS or by Qiagen Therascreen KRAS PCR Kit for mutations in codons 12 and 13. Immunohistochemical analysis also evaluated tumor expression of hypoxia-inducible factor 1 (HIF-1) and minichromosome maintenance protein 2 (mcm2) reflecting tumor hypoxia and proliferation, respectively, features that have both been shown to be of clinicopathologic significance in CRC (24,25). For quantification of immunohistochemical markers, stained slides were examined with an Olympus BX51 microscope. Images were then captured using an Olympus DP20 digital camera and displayed on a computer monitor. For mcm2, 3 separate areas of tumor were analyzed, and cases with greater than 40% of tumor cells positive with mcm2 were scored as positive, the prognostic value of threshold having previously been established for other tumor types (26,27). The HIF-1α score was based on the combined cytoplasmic and nuclear staining as previously described (28). The intensity of cytoplasmic and nuclear staining was graded as either 0 (no staining), 1 (weak staining), or 2 (strong staining). The percentage of tumor cells stained was graded as 1 (<20%), 2 (20%–40%), or 3 (>40%). The product of these 2 values gave the final HIF-1α score.

### Image Acquisition

After a 6-h fast, patients received an intravenous injection of 190 MBq of <sup>18</sup>F-FDG. After an uptake period of 60 min, all imaging was performed on an integrated PET/CT instrument combining PET with a 64-slice multidetector CT (Discovery VCT; GE Healthcare). Low-radiation-dose CT for attenuation correction was performed from the

skull base to upper thigh using the following parameters: 140 kV, 40 mAs, 1.5 pitch, 3.75-mm slice thickness, 5-mm collimation, and 0.98 × 0.98 mm pixel resolution. The PET emission scan was obtained over the same anatomic area. All scans were obtained in 2-dimensional mode, consisting of an emission scan of 8 min/bed position (this protocol being appropriate for the administered activity of <sup>18</sup>F-FDG). PET images were reconstructed with CT for attenuation correction using CT maps. Transaxial emission images of 5.47 × 5.47 × 3.27 mm (in plane matrix size, 128 × 128) were reconstructed using ordered-subsets expectation maximization with 2 iterations and 28 subsets. The axial field of view was 148.75 mm. The DCE CT scan was acquired on the same imaging system immediately after the PET acquisition and comprised a total acquisition time of 150 s in 2 phases after intravenous iohexol (50 mL, 350 mg of iodine per milliliter [Omnipaque; GE Healthcare] at 5 mL/s): an initial phase of 40 s using a 2-s interval between successive images, followed by 110 s with a 5-s interval (120 kV, 60 mA, 9-mSv effective dose; 10-s delay from injection). The cranio-caudal extent of tumor encompassed by the DCE CT acquisition was 4 cm.

### Image Analysis

Multiple-parametric PET/CT image analysis is summarized in Table 1. Each image dataset was analyzed independently by operators masked to the analysis results of the other datasets. Tumor regions of interest (ROIs) enclosing the lesion were constructed from the PET/CT image displaying the largest cross-section area of the CRC tumor using a standardized procedure so that ROIs were comparable in terms of anatomic location for all datasets, as described below.

**<sup>18</sup>F-FDG PET/CT.** The PET emission study and nonenhanced CT were viewed independently and as coregistered studies by a nuclear medicine physician (with > 5 y of experience) using a commercial workstation (Advantage Windows 4.4; GE Healthcare). Maximum standardized uptake value (SUV<sub>max</sub>) for the entire tumor volume was obtained for each patient using an automated thresholding method (Fig. 1).

**CT Texture Analysis (CT TA).** CT TA was performed using TexRAD (TexRAD LTD.; www.texrad.org), a proprietary software algorithm (18,29,30). The texture within CRC tumors was assessed by a medical doctor (with 3 y of experience in constructing tumor ROIs on PET and CT), under the supervision of an imaging researcher (with 7 y of experience in CT TA) and a dual-accredited radiologist/nuclear medicine specialist (with 10 y of PET/CT experience). Tumor ROIs were constructed using the CT images and were refined further by an automatic contouring procedure that excluded gas from the ROI by removing any pixels with attenuation values below -50 Hounsfield units (Fig. 1). Texture within the tumor ROI was quantified after Laplacian of gaussian spatial band-pass image filtration to highlight features with a radius of approximately 5 mm. The mean value of the tumor pixels with positive values (MPP) after filtration was determined using histogram analysis. This parameter, summarized in Equation 1, has previously been shown to correlate negatively with angiogenesis and positively with hypoxia in non-small cell lung cancer (16).

**TABLE 1**  
Summary of Multiparametric Image Analysis

Imaging dataset	Tumor feature	Quantifier
<sup>18</sup> F-FDG PET emission	<sup>18</sup> F-FDG uptake	SUV <sub>max</sub>
Low-dose unenhanced CT	Texture	MPP
DCE CT	Vascularity	BF

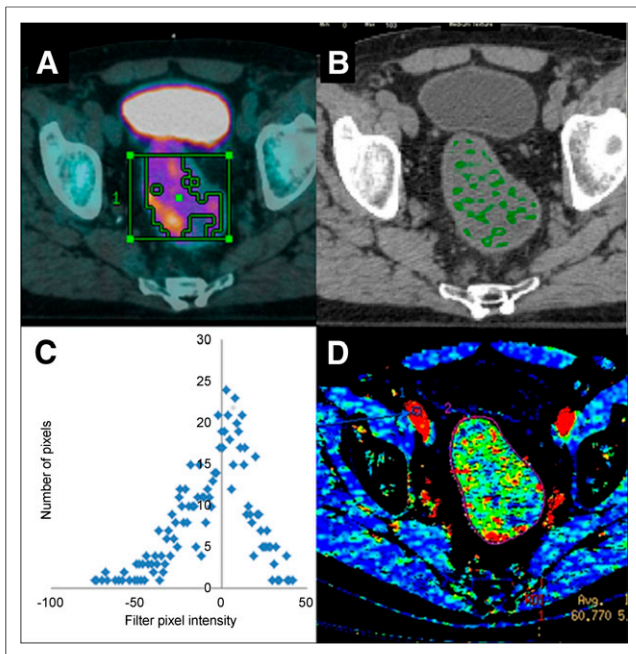


**FIGURE 1.** Multiparametric PET/CT of CRC comprising  $^{18}\text{F}$ -FDG uptake image (A), CT image with positive texture features highlighted by filter shaded green (B), CT texture histogram (C), and CT perfusion image (D). Corresponding values are:  $\text{SUV}_{\text{max}}$ , 10.7; MPP, 12.3; BF, 53.1 mL/min/100 g (text provides methods of derivation).

$$\text{MPP} = \frac{1}{n_+} \sum_{(x,y) \in R} [a_+(x,y)], \quad \text{Eq. 1}$$

where  $R$  is the ROI within the image  $a(x,y)$ ,  $n_+$  is the total number of pixels in  $R$  having positive gray-level values, and  $a_+(x,y)$  is the subset of the image  $a(x,y)$  having only the positive gray-level pixel values.

**DCE CT.** DCE CT data were assessed using software based on distributed parameter analysis (Body Perfusion 3.0; GE Healthcare) (31). A smoothed arterial-time enhancement curve was derived from a circular 20-mm<sup>2</sup> ROI placed within the best-visualized artery, and a blood flow (BF) was parametric map generated. BF averaged over the largest transverse cross-sectional area of tumor was obtained by displaying the defined ROI on the generated parametric map.

#### Decision-Tree and Statistical Analysis

KRAS mutation status was determined for each patient. The true-positive rates (TPRs; that is, the proportion of KRAS mutations testing positive) and false-positive rates (FPRs; that is, the proportion of wild-type tumors testing positive) for mutation detection were then derived for each individual modality as applied to the whole patient cohort. Diagnostic threshold values were determined iteratively to maximize diagnostic accuracy but minimize false-positive diagnoses of KRAS mutation, which, if clinically implemented, could lead to inappropriate withholding of EGFR-targeted therapy. The imaging investigations were applied in order of overall accuracy of detection of the KRAS mutation in the whole cohort. If 2 modalities had the same accuracy, the modality with the lowest FPR was applied first. No further separations of the tree were used if an output arm of a decision node contained only 2 or fewer patients within either diagnostic category (i.e., KRAS mutation or wild-type). The final decision tree was applied to the whole cohort to determine the overall TPR, FPR, and accuracy.

A Monte Carlo analysis using 1,000 iterations of the decision tree was used to assess the impact of uncertainty in the FPR and TPR

for each modality (expressed as their 95% confidence intervals [CIs]) on the overall diagnostic performance of the decision tree. For each iteration, the TPR and FPR for each decision node were randomly selected from a normal distribution with  $\pm 2$  SDs corresponding to the 95% CI. The 5th and 95th percentiles of the resulting 1,000 values for overall TPR, FPR, and accuracy were used to characterize the CIs for the diagnostic performance of the decision tree. Diagnostic performance parameters for the decision tree were compared with the corresponding parameters for each modality applied to the whole cohort. A statistically significant difference was considered present if there was no overlap between the 95% CIs of diagnostic performance parameters. Differences in the expression of HIF-1 and mcm2 between terminal nodes identifying KRAS mutants were assessed using log-rank analysis for multidimensional contingency tables.

## RESULTS

The patient cohort comprised 6 patients with stage 1, 8 with stage 2, 9 with stage 3, and 10 with stage 4 tumors. A KRAS mutation was present in 17 of the 33 cases (51.5%). Fifty-eight percent of tumors stained positively for HIF-1 (median intensity, 1; range, 0–6) and 85% for mcm2. The overall imaging characteristics are summarized in Table 2.

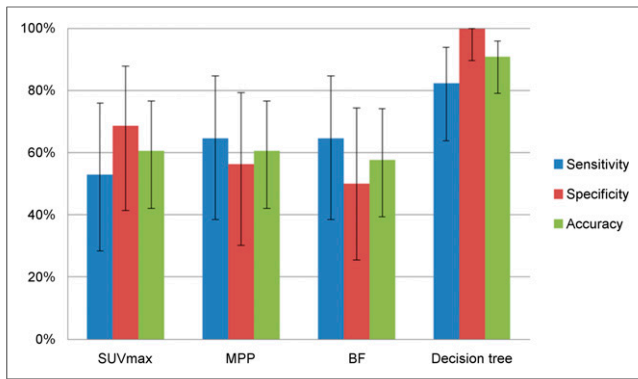
The diagnostic performance parameters for each imaging technique individually applied to the whole cohort are shown in Figure 2. The subsequent decision tree applied  $\text{SUV}_{\text{max}}$  as the initial imaging parameter, having diagnostic accuracy identical to CT TA but lower FPR. CT texture was assessed second. DCE CT was required only to identify KRAS mutations when  $\text{SUV}_{\text{max}}$  was low and MPP high. Thus, the final decision tree comprised 4 decision nodes and 5 terminal nodes (Fig. 3). Table 3 summarizes the TPR and FPR values for each decision node and for the entire decision tree. The individual results from the first 5 iterations of the Monte Carlo analysis are also shown for illustration.

Figure 2 compares the diagnostic performance of the decision tree with that of each modality independently applied to the whole cohort. The TPR, FPR, and accuracy (95% CI) of the decision tree were 82.4% (63.9%–93.9%), 0% (0%–10.4%), and 90.1% (79.2%–96.0%), respectively. The FPR and accuracy values for the decision tree were significantly better than those for each modality applied independently ( $\text{SUV}_{\text{max}}$ , 31.2% [12.1%–58.5%] and 60.6% [42.2%–76.6%]; MPP, 43.7% [20.7%–69.9%] and 60.6% [42.2%–76.6%]; BF, 50.0% [25.5%–74.4%] and 57.6% [39.4%–74.1%]). Mean TPR was greater for the decision tree but with overlap of the 95% CI of each modality applied independently.

The decision tree contained 2 terminal nodes that identified tumors with KRAS mutations. The expression of HIF-1 and mcm2 in tumors identified by these nodes is shown in Table 4. KRAS mutants with high standardized uptake value (SUV) and low MPP values had a significantly increased likelihood of expressing HIF-1

**TABLE 2**  
Summary of Overall Imaging Characteristics

Imaging characteristic	Mean	Range
Tumor area (cm <sup>2</sup> )	11.2	3.5–29.3
$\text{SUV}_{\text{max}}$	18.4	4.5–47.1
MPP	21.6	9.3–138.1
BF (mL/min/100 mL)	77.0	40.5–153.3



**FIGURE 2.** Diagnostic performance values for each modality separately, compared with decision tree.

( $P = 0.032$ ) whereas KRAS mutants with low SUV, high MPP, and high BF expressed mcm2 ( $P = 0.036$ ).

## DISCUSSION

Our study provides an initial demonstration of how multifunctional imaging can potentially be used to assess cancer mutation status. The selection of imaging techniques was hypothesis-driven based on prior knowledge of relevant aspects of tumor biology and their imaging correlates. In this way, not only we were able to identify a potential imaging signature for the KRAS mutation in CRC, but also the additional correlations between imaging and tumor expression of HIF-1 and mcm2 suggested the presence of 2 different imaging phenotypes for the same gene mutation, one hypoxic and the other proliferative. This latter finding illustrates how, by depicting the downstream molecular and physiologic consequences of gene expression, imaging may better reflect tumor phenotype than histologic evaluation of single-gene expression.

By using a recursive decision-tree approach to combine different functional imaging techniques, we were able to identify an imaging signature that identified KRAS mutations with significantly greater accuracy and lower FPR than single imaging techniques, with no reduction in TPR. Although the imaging modalities combined in the decision tree can each provide a range of functional or physiologic measurements, the imaging parameters chosen reflected the relationship that KRAS mutational status exhibits with hypoxia and angiogenesis for which prior studies have shown associations with tumor  $^{18}\text{F}$ -FDG uptake, CT texture expressed as

MPP, and DCE CT measurements of BF in CRC and other tumors (12,16,18,29,30). Recursive decision trees have advantages over other methods for assessing interactions between biomarkers such as linear and proportional hazard models (19). Recursive methods can identify interactions that are predominantly found within a particular range of values and not detected by a simple product or ratio of 2 variables. This benefit is clearly evident in our tree in which the relationship between CT texture and KRAS mutational status is reversed depending on the level of  $^{18}\text{F}$ -FDG uptake within the tumor. Decision trees are also easy to understand and implement by health care professionals (19).

The overall accuracy of multifunctional imaging was sufficiently high (90.1%; 95% CI, 79.2%–96.0%) to indicate a potential clinical role for this technique. The low FPR (0%; 95% CI, 0%–10.4%) would be advantageous for clinical application because false identification of a KRAS mutation could feasibly result in inappropriate withholding of EGFR-targeted therapy. Furthermore, by obtaining all the functional imaging data from a single imaging device (PET/CT), our approach would avoid any inconvenience to patients and additional health care costs that might accrue from use of multiple imaging platforms.

In our series, the accuracy of  $^{18}\text{F}$ -FDG uptake measurements alone was lower than that reported previously (60.6% vs. 75%) despite using a comparable diagnostic threshold ( $\text{SUV}_{\text{max}}$ , 16 vs. 14). The improved accuracy of the decision tree over  $\text{SUV}_{\text{max}}$  measurements alone was achieved in 2 ways: using CT TA to identify wild-type tumors with increased  $^{18}\text{F}$ -FDG uptake and by identifying KRAS mutants with low  $^{18}\text{F}$ -FDG uptake on the basis of CT TA and DCE CT. Thus, the 2 terminal nodes that identify KRAS mutants appear to detect 2 different phenotypes and are supported by the differential expression of HIF-1 and mcm2 associated with these nodes. Mutants with high SUV and low MPP values tended to express HIF-1, implying a hypoxic phenotype. HIF-1 activity increases glucose transporter 1 expression, which is a major determinant of  $^{18}\text{F}$ -FDG uptake. Similarly, low MPP values on CT TA have been found to be associated with hypoxia in non-small cell lung cancer (16). On the other hand, KRAS mutants with low SUV, high MPP, and high BF demonstrated increased mcm2 expression, implying a proliferative phenotype. Unlike some tumors, previous data indicate that  $^{18}\text{F}$ -FDG uptake in primary CRC is unrelated to proliferation (32) whereas a recent study has shown that induction of proliferation in CRC tissue samples did not increase  $^{18}\text{F}$ -FDG uptake (although induction of HIF-1 did increase SUV) (33). Thus, there is concordance between the histologic and imaging findings for both of these subgroups of KRAS mutants. Future studies could usefully explore the relationship between these imaging phenotypic subtypes of KRAS mutations and the genetic subtypes that have recently been shown to differentially predict response to EGFR-targeted therapy (34).

We have shown that imaging may potentially identify different phenotypes associated with the same gene mutation, suggesting a novel but complementary role for imaging as an adjunct to genetic analysis in oncology. Such a role would become clinically important if future studies show that these different imaging phenotypes correspond to different rates of survival or treatment

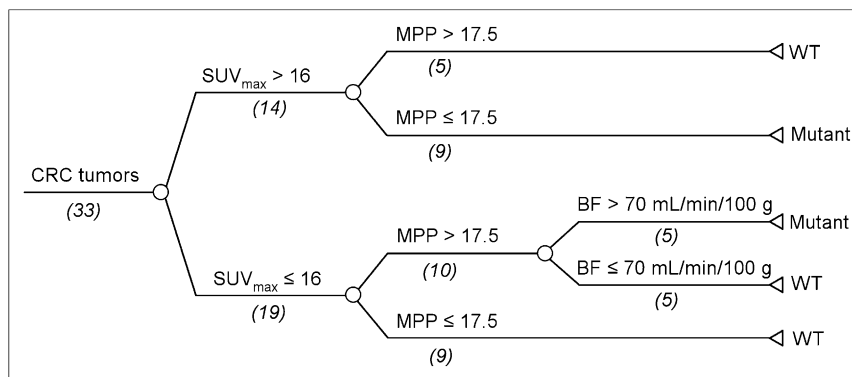


**FIGURE 3.** Summary of decision tree. Numbers in parentheses indicate number of tumors passing along each pathway.

**TABLE 3**  
TPRs and FPRs for Each Decision Node and Entire Decision Tree Along with Their Respective 95% CIs

Parameter/threshold	SUV > 16		MPP ≤ 17.5 (when SUV > 16)		MPP > 17.5 (when SUV ≤ 16)		BF > 70 mL/min/100 mL (when SUV low and MPP high)		Overall decision tree	
	TPR (%)	FPR (%)	TPR (%)	FPR (%)	TPR (%)	FPR (%)	TPR (%)	FPR (%)	TPR (%)	FPR (%)
Baseline	52.9	31.2	100	0	75.0	36.4	83.3	0	82.4	0
95% CI	28.5–76.1	12.1–58.5	62.9–100	0–53.7	35.6–95.6	12.4–68.4	36.5–99.1	0–60.4	63.9–93.9	0–10.4
Iteration 1	49.9	32.6	100	6.0	51.9	30.2	70.1	0	68.1	1.2
Iteration 2	80.7	34.7	85.2	12.3	54.9	21.8	100	0.4	79.4	4.4
Iteration 3	57.0	27.4	100	0	59.6	65.1	80.2	0	77.5	0
Iteration 4	72.1	27.6	90.9	0	69.7	34.9	91.8	26.6	83.4	6.7
Iteration 5	61.3	13.6	96.0	0	69.0	37.2	58.4	0	74.5	0

First 5 iterations of Monte Carlo analysis are also shown.

**TABLE 4**  
Immunohistochemical Differences Between 2 Imaging Phenotypes Identified by Decision Tree

Hypoxia/proliferation	Imaging phenotype	
	SUV > 16, MPP ≤ 17.5	SUV ≤ 16, MPP > 17.5, BF > 70 mL/min/mL
HIF-1 (-)/mcm2 (-)	0	0
HIF-1 (-)/mcm2 (+)	2	4
HIF-1 (+)/mcm2(-)	4	0
HIF-1 (+)/mcm2 (+)	3	1

response. A combined genetic and imaging approach could feasibly be used to select specific therapies for individual patients in a more personalized manner. An imaging signature for the KRAS mutation may also be helpful in planning chemotherapy for those patients for whom histologic analysis has failed because of poor DNA quality in the sample (either because of a small tumor fraction within the biopsy or poor fixation compromising DNA quality). In this scenario, imaging could feasibly be used as an alternative to repeated biopsy. In other circumstances, a discrepancy between the imaging classification of mutational status and that determined by biopsy alone, for example, in a neoadjuvant setting, could trigger rebiopsy to exclude sampling error. Furthermore, for patients with metastatic disease, imaging assessment of KRAS mutational status in individual lesions could feasibly identify specific tumor sites that are more or less likely to respond to specific treatments. For example, lesions predicted as resistant to chemotherapy could be redirected toward more aggressive local treatment such as radiotherapy or ablation.

The main limitation of our study is that work has been exploratory, comprising model building only. The model needs to be externally validated by a subsequent prospective study using a different patient cohort that did not contribute data to model construction, preferably from different institutions. A larger patient cohort would have also narrowed the confidence intervals obtained for the diagnostic performance parameters. Nevertheless, we have presented the largest patient cohort undergoing correlation of KRAS mutational status with combined <sup>18</sup>F-FDG PET, CT TA, and DCE CT reported to date, to our knowledge.

## CONCLUSION

Multiparametric PET/CT with recursive decision-tree analysis to combine measurements of tumor <sup>18</sup>F-FDG uptake, CT texture, and perfusion has the potential to identify imaging signatures for CRCs with KRAS mutations exhibiting hypoxic or proliferative phenotypes.

## DISCLOSURE

The costs of publication of this article were defrayed in part by the payment of page charges. Therefore, and solely to indicate fact, this article is hereby marked "advertisement" in accordance with 18 USC section 1734. This work was undertaken at UCLH/UCL, which received a proportion of the funding from the U.K.'s Department of Health's NIHR Biomedical Research Center's funding scheme. Further funding was received from their NIHR sources. Balaji Ganeshan and Kenneth Miles have a commercial interest in

the tumor textural analysis software through the company TexRAD. No other potential conflict of interest relevant to this article was reported.

## REFERENCES

1. Vogelstein B, Fearon ER, Hamilton SR, et al. Genetic alterations during colorectal-tumor development. *N Engl J Med*. 1988;319:525–532.
2. Lièvre A, Bachet JB, Le Corre D, et al. KRAS mutation status is predictive of response to cetuximab therapy in colorectal cancer. *Cancer Res*. 2006;66:3992–3995.
3. Watanabe T, Kobunai T, Yamamoto Y, et al. Heterogeneity of KRAS status may explain the subset of discordant KRAS status between primary and metastatic colorectal cancer. *Dis Colon Rectum*. 2011;54:1170–1178.
4. Bossard C, Küry S, Jamet P, et al. Delineation of the infrequent mosaicism of KRAS mutational status in metastatic colorectal adenocarcinomas. *J Clin Pathol*. 2012;65:466–469.
5. Richman SD, Chambers P, Seymour MT, et al. Intra-tumoral heterogeneity of KRAS and BRAF mutation status in patients with advanced colorectal cancer (aCRC) and cost-effectiveness of multiple sample testing. *Anal Cell Pathol (Amst)*. 2011;34: 61–66.
6. Pang NK, Nga ME, Chin SY, et al. KRAS and BRAF mutation analysis can be reliably performed on aspirated cytological specimens of metastatic colorectal carcinoma. *Cytopathology*. 2011;22:358–364.
7. Krol LC, 't Hart NA, Methorst N, Knol AJ, Prinsen C, Boers JE. Concordance in KRAS and BRAF mutations in endoscopic biopsy samples and resection specimens of colorectal adenocarcinoma. *Eur J Cancer*. 2012;48:1108–1115.
8. Yang QH, Schmidt J, Soucy G, et al. KRAS mutational status of endoscopic biopsies matches resection specimens. *J Clin Pathol*. 2012;65:604–607.
9. Plesec TP, Hunt JL. KRAS mutation testing in colorectal cancer. *Adv Anat Pathol*. 2009;16:196–203.
10. Sundström M, Edlund K, Lindell M, et al. KRAS analysis in colorectal carcinoma: Analytical aspects of pyrosequencing and allele-specific PCR in clinical practice. *BMC Cancer*. 2010;10:660–668.
11. Roivainen A, Tolvanen T, Salomäki S, et al. <sup>68</sup>Ga-labeled oligonucleotides for in vivo imaging with PET. *J Nucl Med*. 2004;45:347–355.
12. Kawada K, Nakamoto Y, Kawada M, et al. Relationship between <sup>18</sup>F-fluorodeoxyglucose accumulation and KRAS/BRAF mutations in colorectal cancer. *Clin Cancer Res*. 2012;18:1696–1703.
13. Zeng M, Kikuchi H, Pino MS, Chung DC. Hypoxia activates the K-ras proto-oncogene to stimulate angiogenesis and inhibit apoptosis in colon cancer cells. *PLoS ONE*. 2010;5:e10966.
14. Zhang X, Gaspard JP, Chung DC. Regulation of vascular endothelial growth factor by the Wnt and K-Ras pathways in colonic neoplasia. *Cancer Res*. 2001; 61:6050–6054.
15. Kikuchi H, Pino MS, Zeng M, Shirasawa S, Chung DC. Oncogenic KRAS and BRAF differentially regulate hypoxia-inducible factor-1 $\alpha$  and -2 $\alpha$  in colon cancer. *Cancer Res*. 2009;69:8499–8506.
16. Goh V, Engledow A, Rodríguez-Justo M, et al. The flow-metabolic phenotype of primary colorectal cancer: assessment by integrated <sup>18</sup>F-FDG PET/perfusion CT with histopathologic correlation. *J Nucl Med*. 2012;53:687–692.
17. Ganesan B, Ziauddin Z, Goh VJ, et al. Quantitative imaging biomarkers from PET-CT as potential correlates for angiogenesis and hypoxia in colorectal cancer. *Insights Imaging*. 2012;3(suppl 1):S135–S163.
18. Ganesan B, Goh V, Mandeville H, et al. CT of non-small cell lung cancer (NSCLC): histopathologic correlates for texture parameters. *Radiology*. 2013;266: 326–336.
19. Ganesan B, Miles KA, Young RC, Chatwin CR. In search of biologic correlates for liver texture on portal-phase CT. *Acad Radiol*. 2007;14:1058–1068.
20. Singh D, Miles K. Multiparametric PET-CT in oncology. *Cancer Imaging*. 2012;12:336–344.
21. Ruberg SJ, Chen L, Wang Y. The mean does not mean as much anymore: finding sub-groups for tailored therapeutics. *Clin Trials*. 2010;7:574–583.
22. Goh V, Shastry M, Engledow A, et al. Integrated <sup>18</sup>F-FDG PET/CT and perfusion CT of primary colorectal cancer: effect of inter- and intraobserver agreement on metabolic-vascular parameters. *AJR*. 2012;199:1003–1009.
23. Goh V, Rodríguez-Justo M, Engledow A, et al. Assessment of the metabolic flow phenotype of primary colorectal cancer: correlations with microvessel density are influenced by the histological scoring method. *Eur Radiol*. 2012;22:1687–1692.
24. Giaginis C, Georgiadou M, Dimakopoulou K, et al. Clinical significance of MCM-2 and MCM-5 expression in colon cancer: association with clinicopathological parameters and tumor proliferative capacity. *Dig Dis Sci*. 2009;54:282–291.
25. Baba Y, Noshok K, Shima K, et al. HIF1A overexpression is associated with poor prognosis in a cohort of 731 colorectal cancers. *Am J Pathol*. 2010;176:2292–2301.
26. Hashimoto K, Araki K, Osaki M, et al. MCM2 and Ki-67 expression in human lung adenocarcinoma: prognostic implications. *Pathobiology*. 2004;71:193–200.
27. Burger M, Denzinger S, Hartmann A, Wieland WF, Stoehr R, Obermann EC. MCM2 predicts recurrence hazard in stage Ta/T1 bladder cancer more accurately than CK20, Ki67 and histological grade. *Br J Cancer*. 2007;96:1711–1715.
28. Simiantonaki N, Taxeidis M, Jayasinghe C, Kurzik-Dumke U, Kirkpatrick CJ. Hypoxia-inducible factor 1 alpha expression increases during colorectal carcinogenesis and tumor progression. *BMC Cancer*. 2008;8:320.
29. Ganesan B, Panayiotou E, Burnand K, Dizdarevic S, Miles K. Tumour heterogeneity in non-small cell lung carcinoma assessed by CT texture analysis: a potential marker of survival. *Eur Radiol*. 2012;22:796–802.
30. Ganesan B, Abaleke SC, Young RCD, Chatwin CR, Miles KA. Texture analysis of non-small cell lung cancer on unenhanced computed tomography: initial evidence for a relationship with tumor glucose metabolism and stage. *Cancer Imaging*. 2010;10:137–143.
31. St Lawrence KS, Lee TY. An adiabatic approximation to the tissue homogeneity model for water exchange in the brain: I. Theoretical derivation. *J Cereb Blood Flow Metab*. 1998;18:1365–1377.
32. Yamamoto Y, Kameyama R, Izuishi K, et al. Detection of colorectal cancer using <sup>18</sup>F-FLT PET: comparison with <sup>18</sup>F-FDG PET. *Nucl Med Commun*. 2009;30:841–845.
33. Izuishi K, Yamamoto Y, Sano T, et al. Molecular mechanism underlying the detection of colorectal cancer by <sup>18</sup>F-2-fluoro-2-deoxy-D-glucose positron emission tomography. *J Gastrointest Surg*. 2012;16:394–400.
34. De Roock W, Jonker DJ, Di Nicolantonio F, et al. Association of KRAS p.G13D mutation with outcome in patients with chemotherapy-refractory metastatic colorectal cancer treated with cetuximab. *JAMA*. 2010;304:1812–1820.